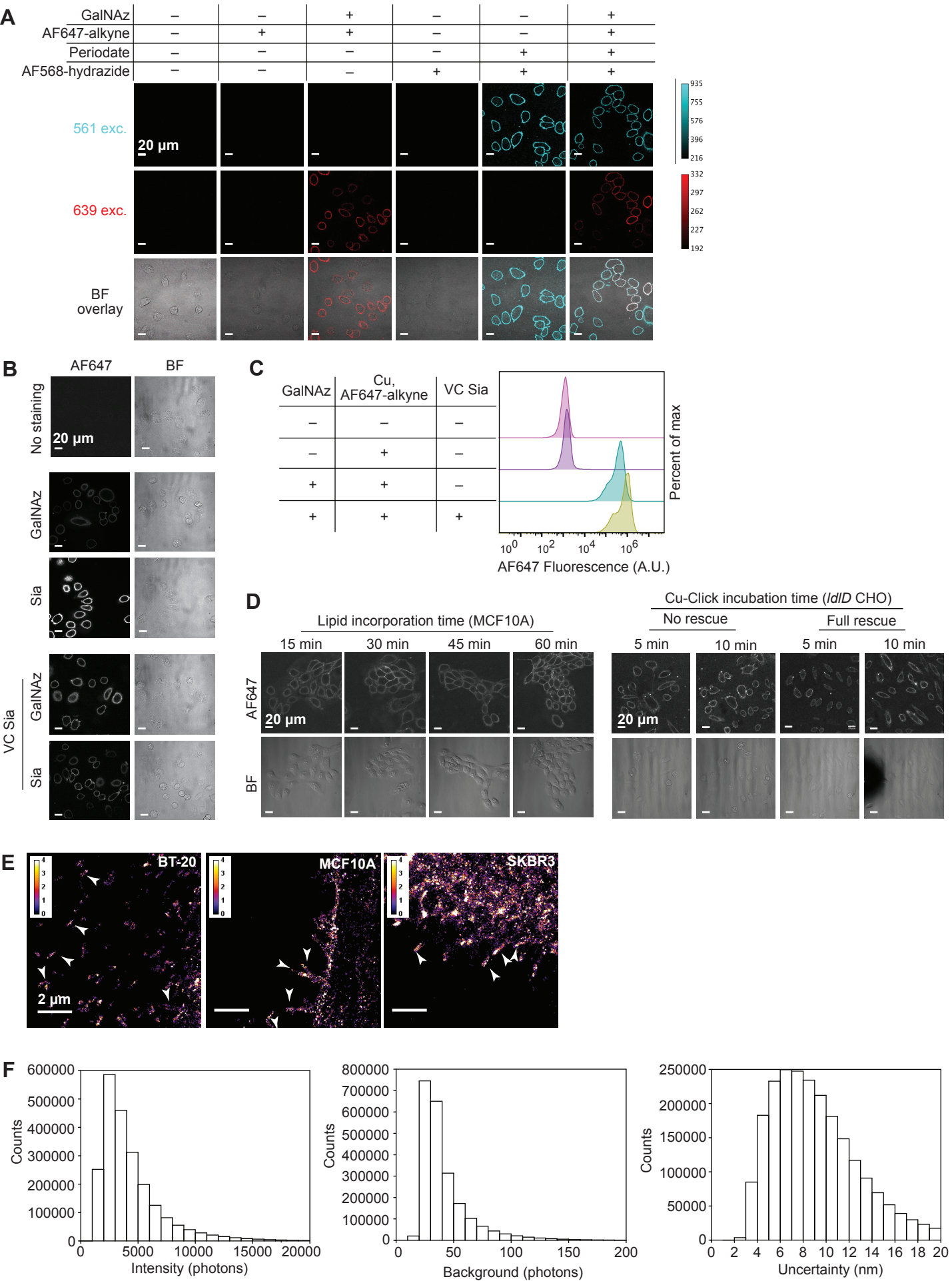
A
GalNAz
AF647-alkyne
Periodate
AF568-hydrazide
561 exc.
639 exc.
BF overlay
20 µm
935
755
576
396
216
332
297
262
227
192
B
AF647
BF
No staining
GalNAz
Sia
VC Sia
C
GalNAz
Cu, AF647-alkyne
VC Sia
Percent of max
AF647 Fluorescence (A.U.)
D
Lipid incorporation time (MCF10A)
15 min
30 min
45 min
60 min
Cu-Click incubation time (IdlD CHO)
No rescue
Full rescue
5 min
10 min
AF647
BF
E
BT-20
MCF10A
SKBR3
2 µm
F
Counts
Intensity (photons)
Background (photons)
Uncertainty (nm)

Figure S1. Validation of labeling workflow. Related to Figure 1.
(A) Confocal images of GalNAz and sialic acid labeling on SKBR3 cells showing various controls. Dye only controls give the expected results, and labeling is consistent across cells in a given field of view. Two-color labeling gives overlaid membrane-localized signal. AF568 hydrazide (Thermo Fisher Scientific) and aminooxy-CF568 can be used interchangeably. Contrast settings are equal for each excitation channel (see lookup tables). (B) Confocal images of SKBR3 cells with and without 30 nM *Vibrio cholerae* sialidase treatment for 2 h at 37 °C (VC Sia). Labeling extend does not decrease for GalNAz labeling, in contrast to Sia labeling. Contrast settings are equal for all fluorescent micrographs. (C) Flow cytometry analysis of the effect of VC Sia treatment on GalNAz labeling. Labeling is not decreased upon exposure of GalNAz labeled SKBR3 cells to VC Sia, as expected. (D) Confocal images of lipid-azide and Cu-click labeled MCF10A MUC1ΔCT (left) and *ldlD* CHO cells grown in media or media supplemented with 10 μM galactose and 100 μM GalNAc (right). For each cell line analyzed with lipid labeling, we screened 15, 30, 45, and 60 minutes incubation with lipid-azide and 5 and 10 minutes Cu-catalyzed click at 4 °C. Conditions giving the best labeling by confocal were used for further analysis. For example, for MCF10A cells (left), lipid incorporation time did not significantly alter the pattern or intensity of labeling, while in the case of *ldlD* CHO cells (right), ten minutes of Cu-catalyzed click resulted in an increase of apparent puncta, which made analysis difficult. Therefore, we chose five minutes of Cu-click labeling time for the *ldlD* CHO cells. Contrast settings are equal for all fluorescent micrographs within each cell line. (E) Representative examples for lipid-labeled tubules on BT-20, MCF10A, and SKBR3 cells. (F) Representative histograms of integrated single-molecule intensity (corresponding to numbers of detected photons with median at 3500), background, and uncertainty of single-molecule localizations. Uncertainties are reported as calculated by ThunderSTORM.

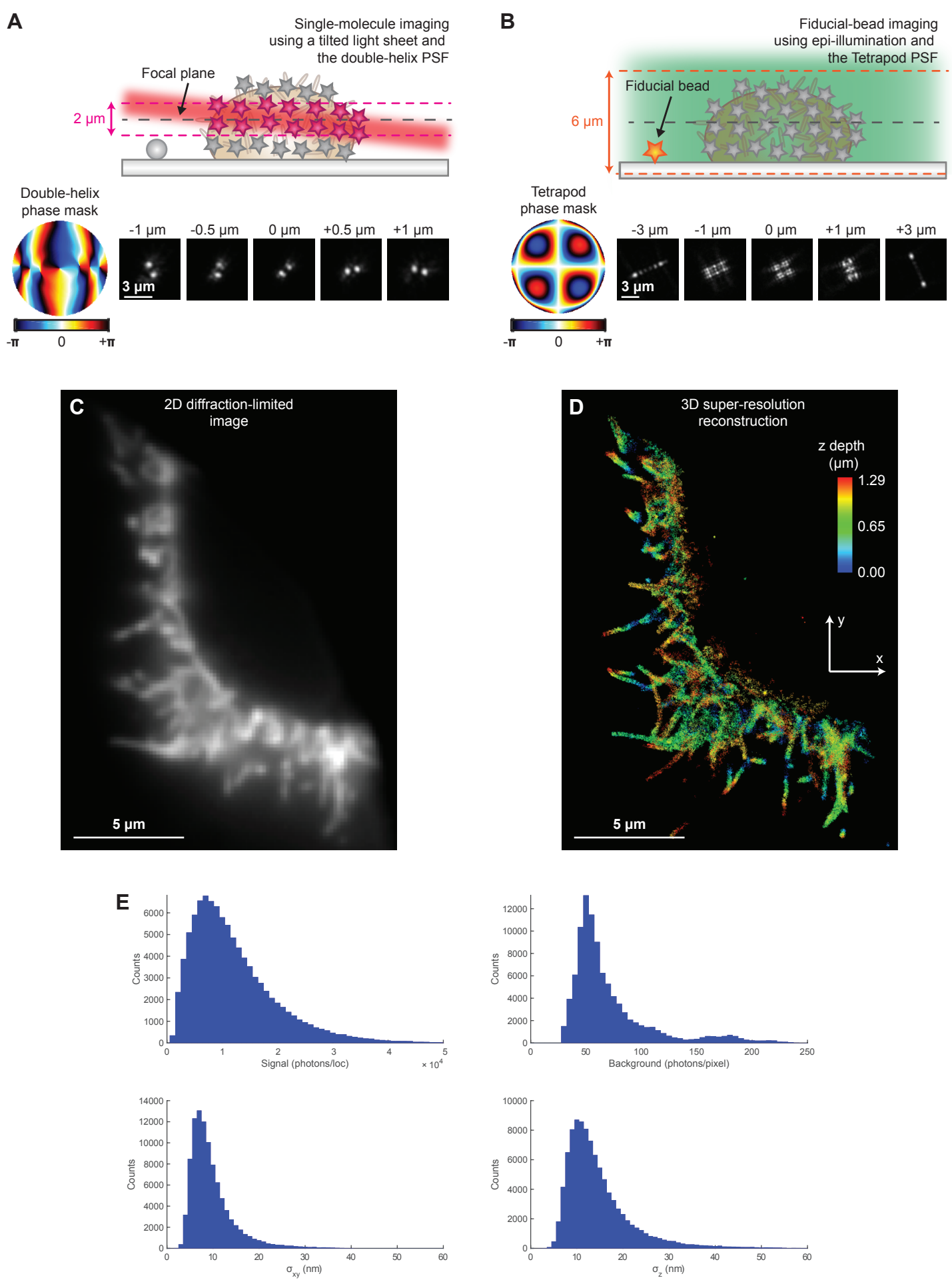
A
Single-molecule imaging
using a tilted light sheet and
the double-helix PSF
Focal plane
2 µm
Double-helix
phase mask
-1 µm
-0.5 µm
0 µm
+0.5 µm
+1 µm
3 µm
-π
0
+π
B
Fiducial-bead imaging
using epi-illumination and
the Tetrapod PSF
Fiducial bead
6 µm
Tetrapod
phase mask
-3 µm
-1 µm
0 µm
+1 µm
+3 µm
3 µm
-π
0
+π
C
2D diffraction-limited
image
5 µm
D
3D super-resolution
reconstruction
z depth
(µm)
1.29
0.65
0.00
y
x
5 µm
E
Counts
Signal (photons/loc)
× 10^4
Background (photons/pixel)
σxy (nm)
σz (nm)

Figure S2. Details of 3D SR microscopy method. Related to Figure 2.
(A) Single AF647 molecules were excited with a tilted light sheet at 647 nm and detected using the double-helix PSF with a 2 μm axial range. (B) Fiducial beads for live and offline drift correction were excited with epi-illumination at 561 nm and detected using the Tetrapod PSF with a 6 μm axial range. (C) 2D diffraction-limited image of the imaged cell. (D) 3D super-resolution reconstruction of the sample. (E) Histograms showing the signal photons per localization, background photons per pixel, and xy and z localization precision from the data shown in Figure 2A and in Figure S2D. The data was filtered to remove localizations with a distance between the two double-helix lobes smaller than 6.1 pixels and larger than 8.0 pixels. Spurious localizations were removed by means of filtering for large average distance to eight nearest neighbors. This resulted in ~100,000 filtered localizations with median photons per localization of 10,298, background photons per pixel of 58, and median localization precision of 8 nm and 13 nm in xy and z, respectively.

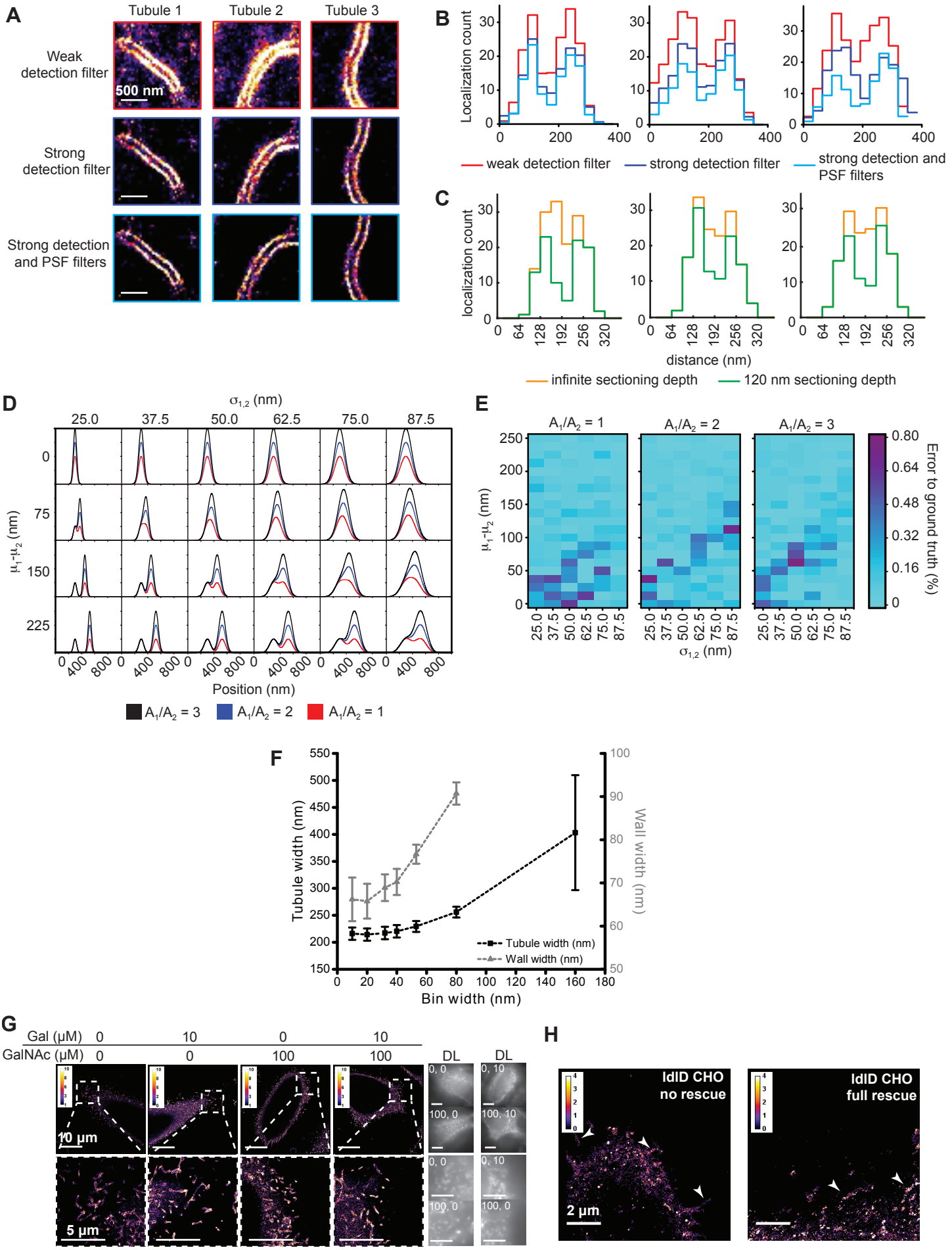
A
Tubule 1
Tubule 2
Tubule 3
Weak detection filter
Strong detection filter
Strong detection and PSF filters
500 nm
B
Localization count
weak detection filter
strong detection filter
strong detection and PSF filters
C
localization count
distance (nm)
infinite sectioning depth
120 nm sectioning depth
D
σ1,2 (nm)
25.0
37.5
50.0
62.5
75.0
87.5
μ1-μ2 (nm)
Position (nm)
A1/A2 = 3
A1/A2 = 2
A1/A2 = 1
E
A1/A2 = 1
A1/A2 = 2
A1/A2 = 3
μ1-μ2 (nm)
σ1,2 (nm)
Error to ground truth (%)
F
Tubule width (nm)
Wall width (nm)
Bin width (nm)
G
Gal (μM)
GalNAc (μM)
DL
10 μm
5 μm
H
IdlD CHO no rescue
IdlD CHO full rescue
2 μm

Figure S3. Benchmarking of tubule analysis routine. Related to Figure 3.
(A) Three example tubules taken from experimental SR reconstructions presented with various filtering settings. Top: weak threshold for point spread function (PSF) detection; middle: restrictive threshold for PSF detection; bottom: restrictive threshold and additional filtering post-reconstruction, removing localizations with a localization precision above 20 nm and PSFs with a width above 200 nm on the camera. The last, strong filtering was used for all experimental data presented in this work. By visual inspection, as the filtering becomes more restrictive, the tubules are resolved more clearly as hollow. (B) Line profiles corresponding to the three tubules shown in Figure S3A at the three filtering strengths, confirming the visual impression from Figure S3A. Thus, the ability to resolve the tubules as hollow is a result of quasi-sectioning due to rigid detection and filtering of the PSFs. This is expected as the localizations that would be projected to the middle of the tubule are the ones that are most out of focus, that is, they exhibit larger PSFs on the camera and, as a result of spreading the photons over a larger area, appear dimmer, leading to larger localization uncertainty. Hence, they are either (i) not detected in the first place due to rigid detection threshold or (ii) removed by the filter for small PSF widths or (iii) removed by the filter for small uncertainties. (C) To estimate the achieved quasi-sectioning depth, we simulated the three tubules depicted in Figure S3B as hollow cylinders using the procedure described in Figure 3A. We projected the localizations onto the xy plane assuming various sectioning depths. We binned the localizations into histograms with a bin width of 32 nm (the pixel size of the SR reconstructions) and extracted the line profile along the transverse dimension of the tubule to resemble the experimental situation. The experimental line profile using the strongest filtering conditions (light blue profile in Figure S3A) was best matched by a sectioning depth of 120 nm (compare light blue line profiles in Figure S3B and green line profiles in S3C). For comparison, the yellow line profile in Figure S3C depicts infinite sectioning depth. (D) To ensure that the double Gaussian fit is able to recover the tubule width robustly we simulated ground truth double Gaussian profiles. For this, two single Gaussian profiles were summed. The distance between their centers was changed from 0 to 250 nm in steps of 25 nm. Also, the standard deviations and amplitude ratios between the two Gaussians were varied from 25 to 87.5 nm in 12.5 nm steps and set to 1, 2, or 3, respectively. This parameter space resulted in a broad range of simulated profiles that spanned from two well-separated single-Gaussian profiles, partly overlapping profiles with shoulders, to completely overlapping profiles that were visually indistinguishable from single Gaussian profiles. (E) Each of the ground truth profiles shown in Figure S3D, with 10% noise added relative to an amplitude of one to account for random fluctuations, was fitted to a double Gaussian, the predicted tubule width was obtained, and the absolute error between the prediction and the ground truth tubule width was calculated, shown here. Evidently, the fit is able to extract the true width of the simulated profiles. None of the tested conditions exhibited an error exceeding 0.8% which corresponds to fractions of a nanometer. Hence, we are confident that the double Gaussian fit is a robust tool to determine the tubule width from the SR data, in spite of the fact that not all tubules are resolved as hollow. (F) Relation between the determined tubule width and the pixel size of the reconstruction. As we used 2D histograms to reconstruct the SR data for later tubule analysis, we wanted to ensure that the chosen bin width of 32 nm does not bias the results of the tubule and wall width measurements. Thus, we reconstructed the same set of localizations with different bin widths, analyzed identical tubules, and compared the results. The tubule widths are robustly determined with bin widths between 10-40 nm. Error bars: SEM. (G) SR reconstructions of *ldlD* CHO cells. (H) Representative examples for lipid-labeled tubules on *ldlD* CHO cells.

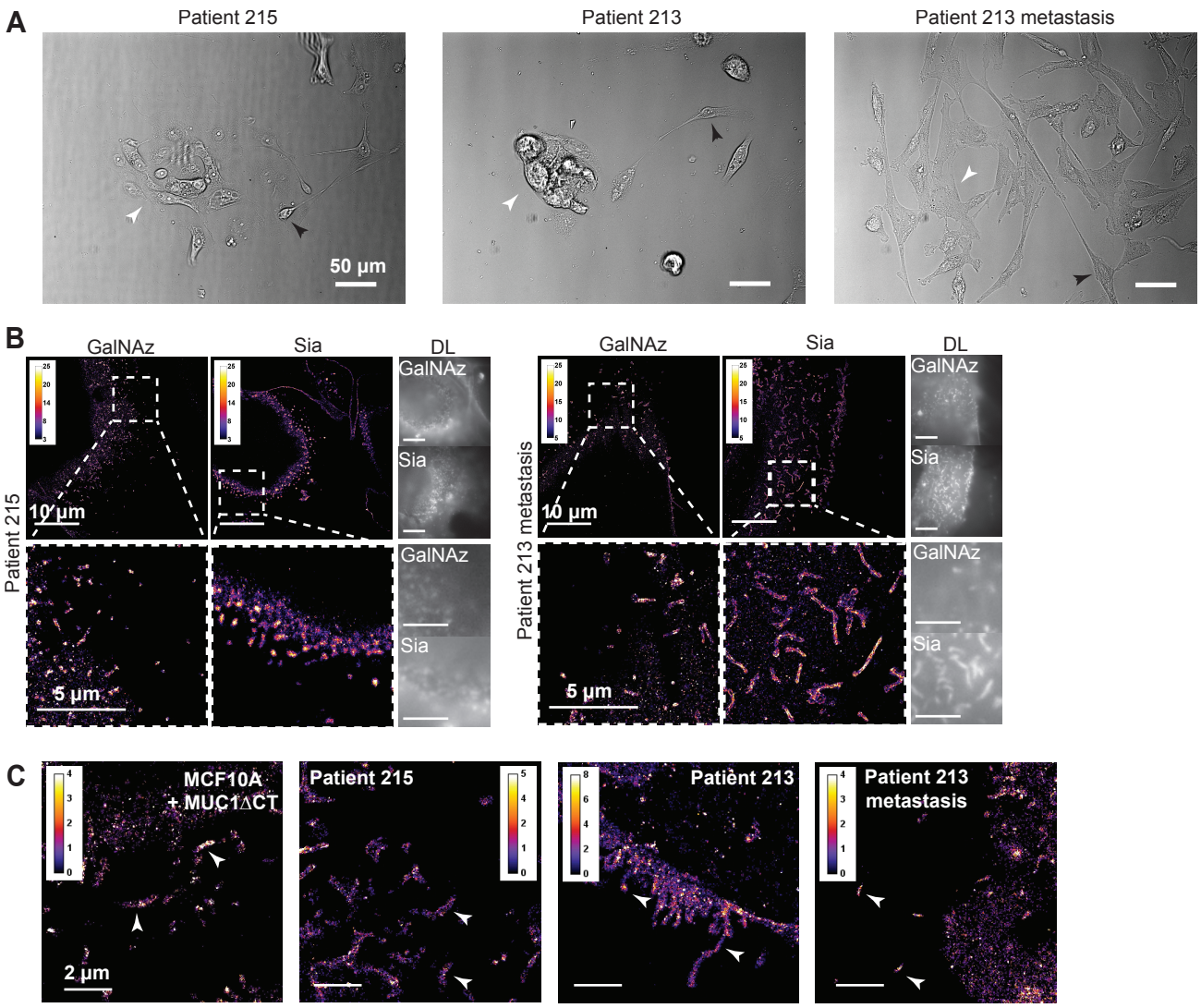
A
Patient 215
Patient 213
Patient 213 metastasis
50 µm
B
GalNAz
Sia
DL
Patient 215
Patient 213 metastasis
10 µm
5 µm
C
MCF10A
+MUC1ΔCT
Patient 215
Patient 213
Patient 213
metastasis
2 µm

Figure S4. Imaging of patient-derived samples. Related to Figure 4.
(A) Representative bright-field images of Patient 215, Patient 213, and Patient 213 metastatic cells. The morphological difference between tumor cells in small colonies (white arrowheads) and spindle-like non-tumor cells (black arrowheads) is evident. Note also that non-tumor cells did not exhibit tubules when examined by SR microscopy. (B) Representative SR reconstructions for GalNAz- and Sia-labeled Patient 215 cells (left), and Patient 213 metastatic cells (right). (C) Representative examples for lipid-labeled tubules on MCF10A+MUC1ΔCT, Patient 215, Patient 213, and Patient 213 metastatic cells. Arrowheads show exemplary tubules.

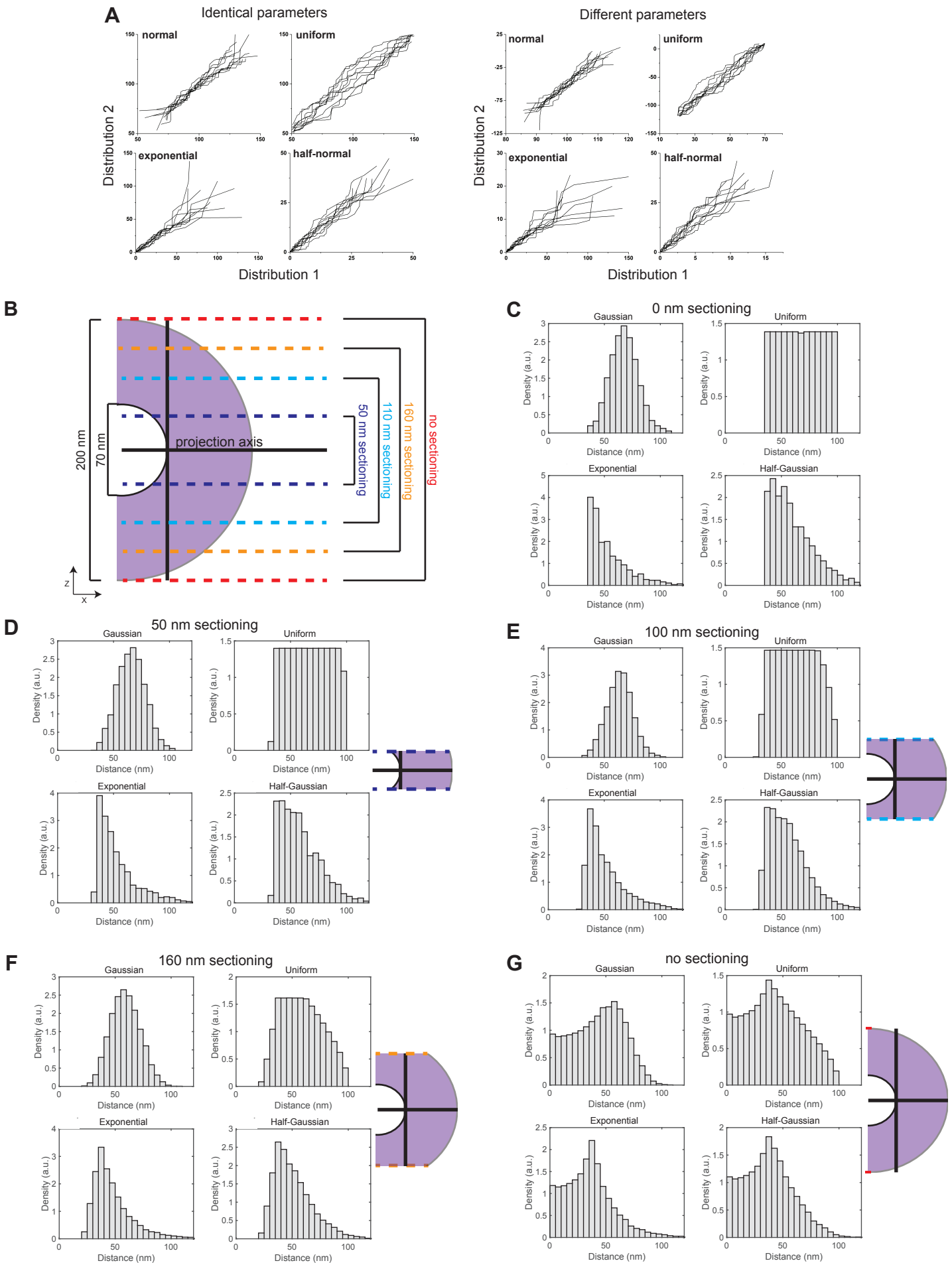
A
Identical parameters
Different parameters
normal
uniform
exponential
half-normal
Distribution 2
Distribution 1
B
200 nm
70 nm
projection axis
50 nm sectioning
110 nm sectioning
160 nm sectioning
no sectioning
z
x
C
0 nm sectioning
D
50 nm sectioning
E
100 nm sectioning
F
160 nm sectioning
G
no sectioning
Gaussian
Uniform
Exponential
Half-Gaussian
Density (a.u.)
Distance (nm)

Figure S5. Projection does not affect QQ analysis. Related to Figure 5.
(A) QQ plots of 20 pairwise compared Gaussian, uniform, exponential, and half-Gaussian distributions with identical (left) and different (right) parameters. A linear trend is observed in all cases. Thus, parameter values do not influence the QQ analysis. Note that the spread in the data is larger where the probability density of the underlying distribution is low, that is, where a single event has a higher impact. This effect is absent for the uniform distribution, which has a constant probability density. (B) To investigate the effect of projection on the QQ-analysis, we simulated a tubule as a hollow cylinder with an inner diameter of 70 nm and an outer diameter of 200 nm, corresponding to typical experimentally measured widths of lipid-labeled and Sia-labeled tubules. We assigned to the simulated glycocalyx a continuous density of localizations corresponding to each of the four distributions investigated (Gaussian, uniform, exponential, and half-Gaussian). (C)-(G) We projected the localization densities around the tubule using axial sectioning depths of 0 nm (C), 50 nm (D), 110 nm (E), 160 nm (F), and infinite sectioning (G). The projected localizations were binned. For visual reference, the region of the tubule corresponding to the specific sectioning depth is shown in purple next to the histograms. Inspection of the histograms confirm that sectioning depths up to 160 nm (compare histograms in (C) to (F)) do not significantly distort the shape of the four distributions, that is, the three-dimensional ground-truth density is preserved in the projection. Only for very large sectioning depths, the shape is significantly altered, and importantly, the resulting projected densities do not resemble any of the four investigated distributions (G). Thus, agreement between the experimental and any of the four model distributions cannot be explained by projection. In summary, considering our estimated sectioning depth of approximately 120 nm, we can conclude that projection does not have a strong effect on the QQ-analysis.

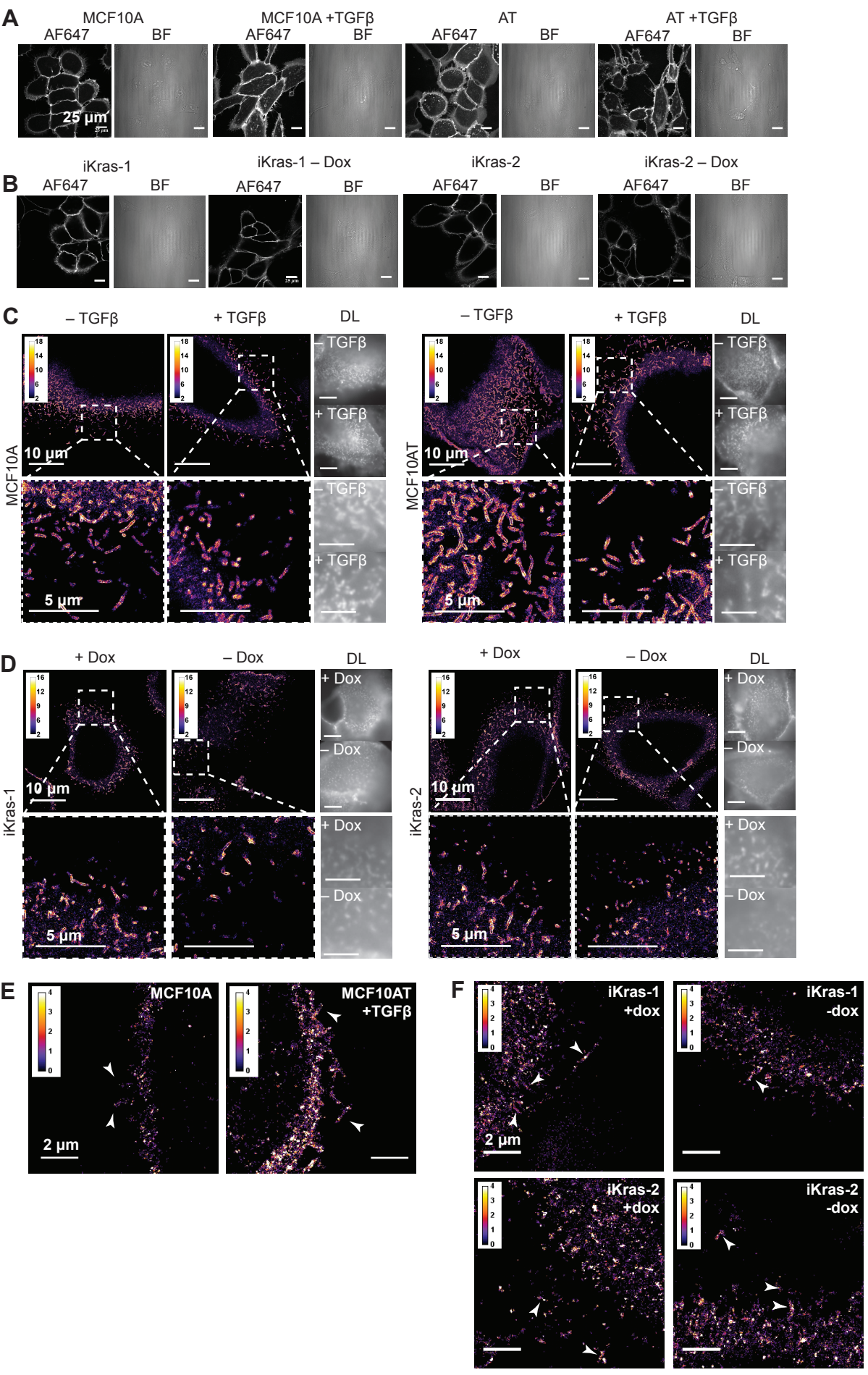
A
MCF10A
MCF10A +TGFβ
AT
AT +TGFβ
AF647
BF
25 μm
B
iKras-1
iKras-1 – Dox
iKras-2
iKras-2 – Dox
C
– TGFβ
+ TGFβ
DL
MCF10A
MCF10AT
10 μm
5 μm
D
+ Dox
– Dox
iKras-1
iKras-2
E
MCF10A
MCF10AT +TGFβ
2 μm
F
iKras-1 +dox
iKras-1 -dox
iKras-2 +dox
iKras-2 -dox

Figure S6. Imaging of MCF10A panel and iKras panel. Related to Figure 6.
Confocal images of the (A) MCF10A panel and (B) iKras panel. Labeling is consistent throughout a given field of view. Gross morphological changes are evident. Representative examples for SR reconstructions of cells from the (C) MCF10A panel and (D) iKras panel. Throughout all cells, a high number of well-resolved glycocalyx-covered tubules were found. Representative examples for lipid-labeled tubules on the (E) MCF10A panel and (F) iKras panel. Arrowheads show exemplary tubules.

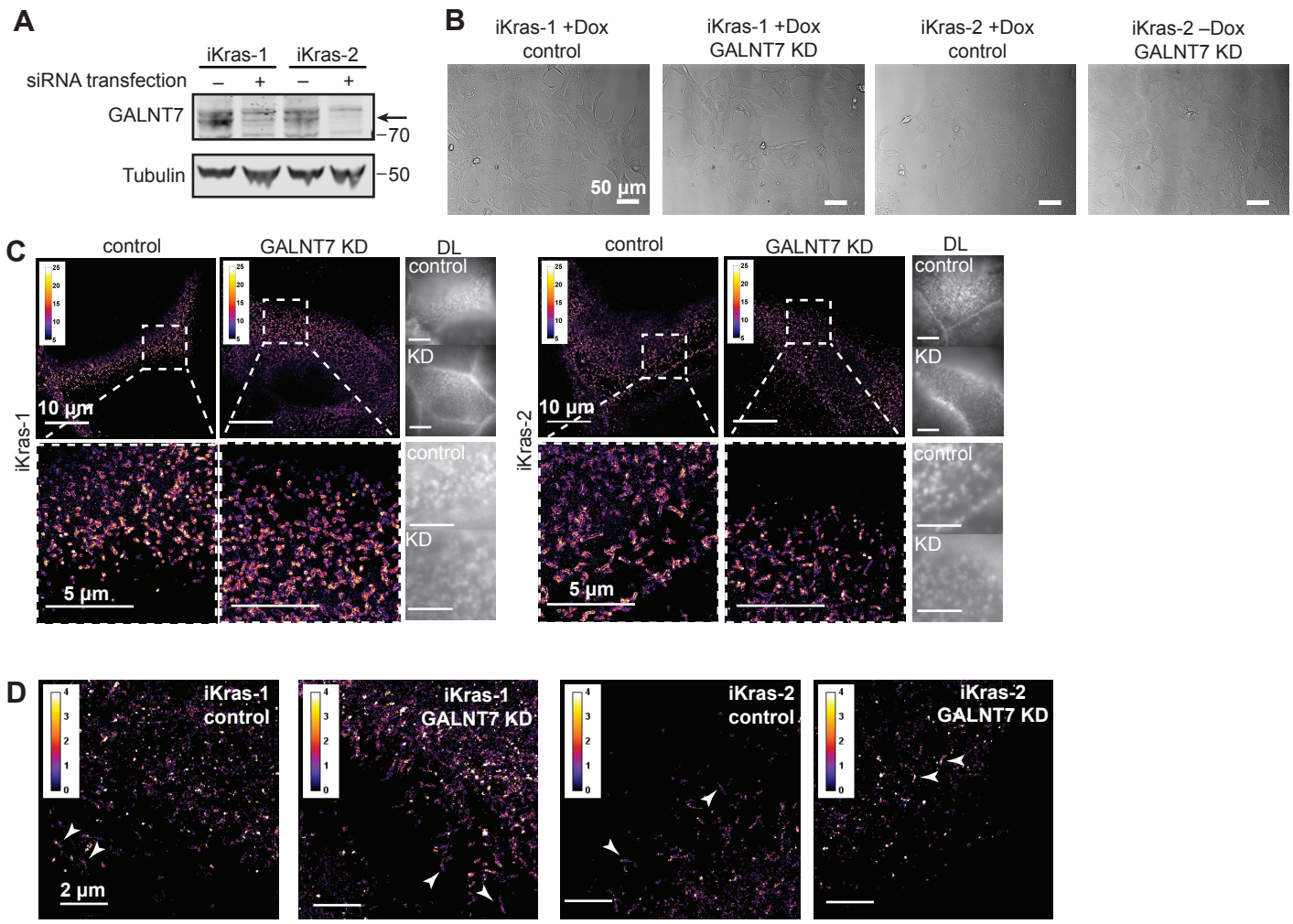
A
iKras-1
iKras-2
siRNA transfection
– + – +
GALNT7
70
Tubulin
50
B
iKras-1 +Dox
control
iKras-1 +Dox
GALNT7 KD
iKras-2 +Dox
control
iKras-2 –Dox
GALNT7 KD
50 μm
C
control
GALNT7 KD
DL
control
KD
iKras-1
iKras-2
10 μm
5 μm
D
iKras-1
control
iKras-1
GALNT7 KD
iKras-2
control
iKras-2
GALNT7 KD
2 μm

Figure S7. Imaging and blots of iKras-1/2 knockdown lines. Related to Figure 7.
(A) Western blot analysis of dox-induced iKras-1 and -2 cell lines transfected with 100 nM siRNA pool targeting *GALNT7*. Arrow indicates GALNT7 band. The low affinity of the GALNT7 antibody necessitated loading of greater than 50 ng protein onto the gel, resulting in poorly resolved tubulin bands. (B) Bright field images of dox-treated iKras-1 and iKras-2 cells with and without *GALNT7* knockdown reveal no visible morphological changes. (C) Representative examples for SR reconstructions of dox-treated iKras-1 and iKras-2 cells with and without *GALNT7* knockdown. All cells exhibit a high number of well-resolved glycocalyx-covered tubules. (D) Representative examples for lipid-labeled tubules on dox-treated iKras-1 and iKras-2 cells with and without *GALNT7* knockdown.